



Article

An Adaptive Thresholding Approach toward Rapid Flood Coverage Extraction from Sentinel-1 SAR Imagery

Shujie Chen ¹, Wenli Huang ^{1,2,*} , Yumin Chen ¹ and Mei Feng ¹

¹ School of Resource and Environmental Sciences, Wuhan University, Wuhan 430079, China; chenshujie2016@whu.edu.cn (S.C.); ymchen@whu.edu.cn (Y.C.); fengmei2016@whu.edu.cn (M.F.)

² Key Laboratory of Urban Land Resources Monitoring and Simulation, Ministry of Land and Resources of China, Shenzhen 518034, China

* Correspondence: wenli.huang@whu.edu.cn; Tel.: +86-027-68778381

Abstract: Flood disasters have a huge effect on human life, the economy, and the ecosystem. Quickly extracting the spatial extent of flooding is necessary for disaster analysis and rescue planning. Thus, extensive studies have utilized optical or radar data for the extraction of water distribution and monitoring of flood events. As the quality of detected flood inundation coverage by optical images is degraded by cloud cover, the current data products derived from optical sensors cannot meet the needs of rapid flood-range monitoring. The presented study proposes an adaptive thresholding method for extracting water coverage (AT-EWC) regarding rapid flooding from Sentinel-1 synthetic aperture radar (SAR) data with the assistance of prior information from Landsat data. Our method follows three major steps. First, applying the dynamic surface water extent (DSWE) algorithm to Landsat data acquired from the year 2000 to 2016, the distribution probability of water and non-water is calculated through the Google Earth Engine platform. Then, current water coverage is extracted from Sentinel-1 data. Specifically, the persistent water and non-water datasets are used to automatically determine the type of image histogram. Finally, the inundated areas are calculated by combining the persistent water and non-water datasets and the current water coverage as derived from the above two steps. This approach is fast and fully automated for flood detection. In the classification results from the WeiFang and Ji'An sites, the overall classification accuracy of water and land detection reached 95–97%. Our approach is fully automatic. In particular, the proposed algorithm outperforms the traditional method over small water bodies (inland watersheds with few lakes) and makes up for the low temporal resolution of existing water products.

Keywords: flood disasters; Sentinel-1; SAR; thresholding; water probability



Citation: Chen, S.; Huang, W.; Chen, Y.; Feng, M. An Adaptive Thresholding Approach toward Rapid Flood Coverage Extraction from Sentinel-1 SAR Imagery. *Remote Sens.* **2021**, *13*, 4899. <https://doi.org/10.3390/rs13234899>

Academic Editors: Guy Schumann and Fumio Yamazaki

Received: 26 October 2021

Accepted: 28 November 2021

Published: 2 December 2021

Publisher's Note: MDPI stays neutral with regard to jurisdictional claims in published maps and institutional affiliations.



Copyright: © 2021 by the authors. Licensee MDPI, Basel, Switzerland. This article is an open access article distributed under the terms and conditions of the Creative Commons Attribution (CC BY) license (<https://creativecommons.org/licenses/by/4.0/>).

1. Introduction

Flood disasters are high-frequency events with a wide influence, causing serious impacts on ecological environments, human societies, and economies. Accurately and quickly evaluating the location, scope, and intensity of flood disasters is necessary for disaster analysis and rescue planning [1]. Disaster assessment is based on the inundation range of the flood disaster. As an advanced and widely used technology, remote sensing is eminently suitable for assessing flood coverage [2]. In remote-sensing images, floods are characterized by clear boundaries. Therefore, many recent studies have extracted flooded coverage from satellite data [3,4]. Satellite-based remote sensing has become an important part of earth observation. Besides providing high spatial, spectral and temporal resolution, it has been developed on multiple platforms and sensors [5]. Among these developments, multispectral, thermal and radar data are the main supports for flood coverage extraction [6,7]. Multispectral and thermal data, such as those drawn from Landsat and MODIS, are widely used and have resulted in a variety of products [8,9]. For example, Landsat data were used to generate an analysis ready dataset (ARD) using the dynamic surface water extent (DSWE) algorithm, developed by the United States Geological

Survey (USGS), for the US and its territories [10], global surface water (GSW) [11], and the global 3-s/1-s water body map (G3WBM/G1WBM) [12].

Synthetic aperture radar (SAR), which is less susceptible to cloud interference than optical data, is promising as a means of monitoring the temporal and spatial changes in flood extent [13]. Three major development stages were enabled by using SAR data for flood monitoring. In the early era of flood analysis, coarse-resolution single-polarized SAR data were used to extract texture features and water-area backscatter for flood detection [14,15]. Using SIR-C and 100-m resolution JERS-1 L-band data, Hess et al. achieved a 62% user accuracy for flood detection in the Amazon River at low water levels and 86% at high water levels [16]. Henry et al. [17] analyzed one multi-polarized ASAR data set, highlighting the greater capability of the Envisat ASAR instrument for flood mapping, particularly the benefits of combining similarity and cross-polarization for rapid mapping in crises. Recently, multi-temporal SAR data, with less than 10 m spatial resolution, provided the ability to monitor the flood event within hours of a disaster. Martinis et al. developed a real-time automatic flood detection tool using segmented histogram thresholding for high-resolution TerraSAR-X SAR data (3 m) [18]. Mason et al. also focused on high-resolution TerraSAR-X data and proposed a semi-automatic algorithm for flood detection in urban areas [19,20]. Tanguy et al. tested and evaluated two case studies of the 2011 Richelieu River flood using the t-resolution data (3 m) [21]. Pulvirenti et al. analyzed the flood situation after the 2011 tsunami that hit Japan, using COSMO-SkyMed data [22]. Multiple authors proposed methods for flood extraction using Sentinel-1 SAR data. Twele et al. presented an automated Sentinel-1-based processing chain designed for flood detection and monitoring in near-real-time (NRT) [23]. Indeed, super-high-resolution sensors, such as ICEYE, could collect worldwide daily SAR data at 0.25 m spatial resolution for ice management use [24]. However, to date, the ICEYE data has not been freely available.

Flood coverage extraction from radar data has gradually increased over the years, and various extraction methods have become available [25,26]. On the one hand, thresholding is one of the most widely used approaches to delineating water extent because of its effectiveness and efficiency [27]. In digital image processing, thresholding is the simplest method of segmenting images. Currently, the most commonly used segmenting images methods include superpixel segmentation methods [28,29], watershed segmentation methods [30,31], and level set segmentation methods [32,33]. The classic threshold methods used in flood coverage extraction from radar data include the Otsu method (maximizing inter-class variance) [6], the entropy threshold method [34,35], and the bimodal histogram method [36]. Many scholars have conducted research based on threshold methods. Sekertekin et al. investigated the performance of fifteen automatic thresholding methods and summarized the advantages and disadvantages of each method and the scope of application [37]. Wang et al. presented a water-body detection framework with an automatic threshold determination procedure [38]. Liang et al. proposed a local thresholding method for water delineation [39]. However, the method required a long time for processing complex images [40]. Moreover, accurate thresholds are difficult to determine because test areas are widely variable. The accuracy of the threshold method depends on the size of the water area in the image. If the grayscale histogram is unimodal, the threshold is difficult to detect [41]. On the other hand, machine learning methods have achieved accurate extraction results and improved handling of the influence of noise [42]. Shahabi et al. proposed a new flood mapping technique based on bagging as a meta-classifier and K-nearest neighbor (KNN), using Sentinel-1 for flood mapping [43]. Lv et al. combined the gray-level co-occurrence matrix (GLCM) and the support vector machine (SVM) to extract the target area of the water and, based on the gray information and the spatial distribution information of the pixels, calculated GLCM texture features in four spatial directions [44]. However, the parameters greatly affect the classification results, so much calculation and debugging are required. The training dataset is difficult to obtain, and the classifier training is time-consuming [45,46]. Random forests (RF) is a supervised machine learning algorithm that has recently started to gain prominence in water resources applications. Tyrallis et al. reviewed RF applications in

water resources, highlighting the potential of the original algorithm and its variants, and assessed the degree of RF exploitation in a diverse range of applications [47]. Considering the advantages and disadvantages of the two mainstream methods, the current research automates the threshold selection and improves the accuracy and speed of extraction. For the benefit of retrieval, our investigation of method comparison is concisely summarized in Table 1.

Table 1. Summary of water bodies extraction method from radar data.

Method	Category	Pros and Cons	Example
Image Thresholding	Otsu Binarization	an exhaustive algorithm for searching the global optimal threshold; easy to be severely corrupted by noise	[6,27,48,49]
	Entropy Threshold	features are easy to select and replace; a large amount of computation	[34,35,40,50]
	Bimodal Histogram	effectiveness and efficiency; strict requirements are necessary for the shape of the histogram; low applicability	[50–52]
Machine Learning	Support Vector Machine (SVM)	achieves accurate extraction results and improves the influence of noise; the parameters greatly affect the classification results	[44,45,53]
	K-Nearest Neighbor (KNN)	decrease the overfitting and variance problems in the training dataset; a large amount of calculation and debugging is required	[43,54]
	Random Forest (RF)	the most accurate method for the classification of water bodies at present; a training dataset is difficult to obtain, and the classifier training is relatively time-consuming	[45,47,55–57]

The contributions of this work are summarized as follows.

1. A fully automated thresholding method was developed for extracting flood ranges with higher temporal resolution. Existing global water monitoring products are mostly generated by optical remote sensors. There are also annual composite data because of the influence of cloud cover. The inundation area during the flood period can be ascertained by our method, which makes up for the lack of temporal resolution of optical products.
2. The proposed method is tested over reservoir and watershed study sites in China. The area of water and non-water can be extracted quickly and accurately with our fully automated approach. The classification results of the two types of sites also show that our method is better than existing thresholding methods (e.g., Otsu [6]).

This paper is organized into six sections. Section 2 introduces the study area and data used in the paper. Section 3 describes the main process of the proposed approach in detail. Experimental results at two sites are presented in Section 4, demonstrating the feasibility and superiority of the proposed approach. Section 5 discusses the advantages and limitations of the method and the future development. Section 6 draws a conclusion regarding our work.

2. Study Area and Data

2.1. Study Area

As experimental sites representative of inland and coastal waters in China, WeiFang City in Shandong Province and Ji'An City in Jiangxi Province were selected, respectively (Figure 1). WeiFang is in the north-central part of Shandong Province and has a continental climate, being in a warm temperate monsoon zone. Floods are common from June to August, and many reservoirs and small lakes exist in the area. Ji'An is in the middle of Jiangxi Province and has a humid subtropical monsoon climate. This site is to be found in the Ganjiang River Basin and is shown as a linear river on images.

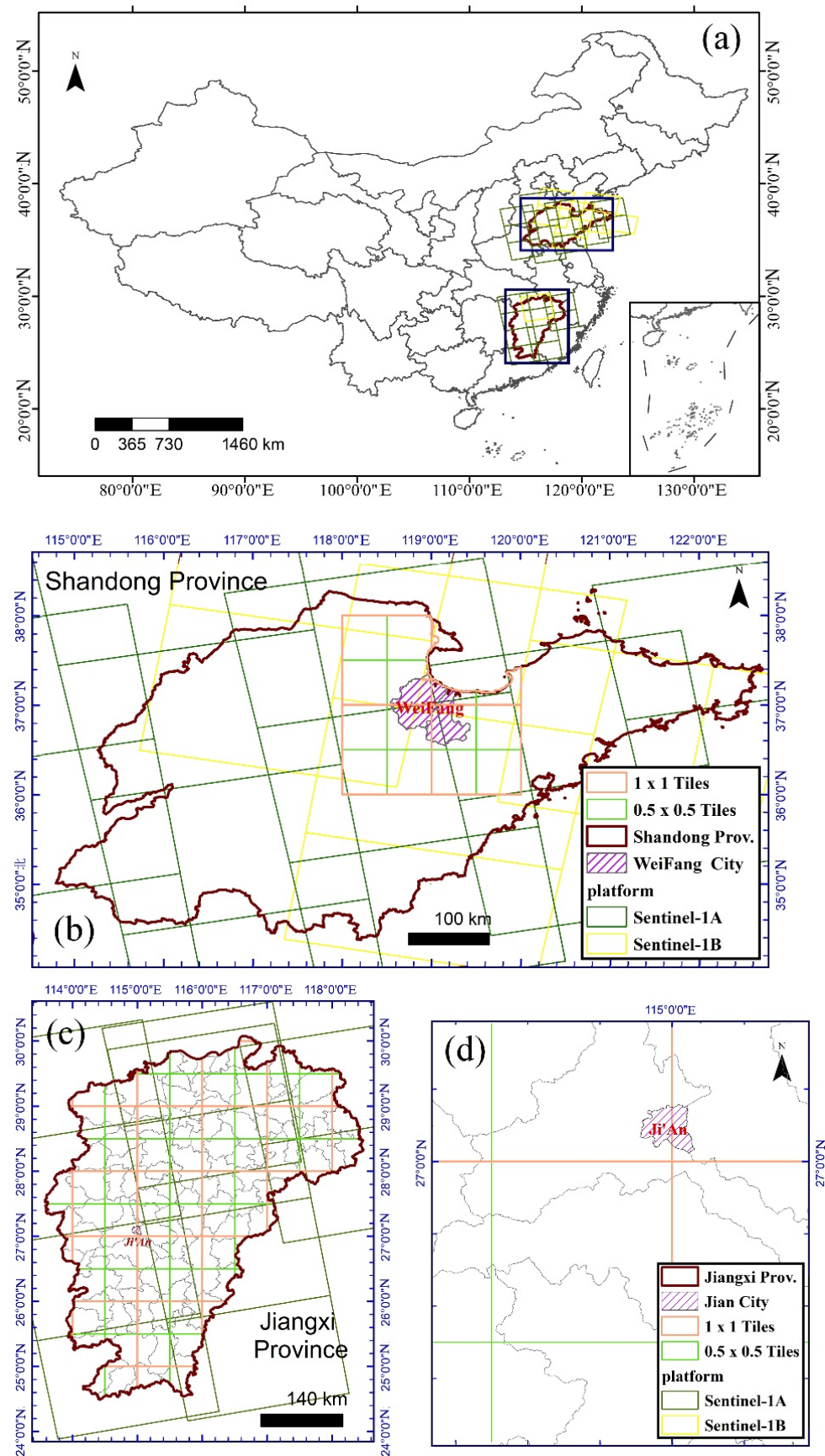


Figure 1. Map of the study sites: locations of (a) the two provinces in China, (b) WeiFang in Shandong Province, (c) Jiangxi Province, and (d) Ji'An City.

2.2. Remote-Sensing Datasets

2.2.1. Sentinel-1 Data

Since 2014, the European Space Agency (ESA) has freely provided its Sentinel-1 C-band SAR satellite data to the world. Sentinel satellites are the first projects for environmental monitoring and safety monitoring that are sponsored by ESA, and Sentinel-1 is one of six satellites now in service. The Sentinel-1 satellite is equipped with a C-band radar imaging system. A single satellite can map the whole world once every 12 days. In dual operation, satellites Sentinel-1A and -1B shorten the revisit period to six days (three days in the equatorial region) [58], realizing continuous monitoring of the surface water range. Sentinel-1 operates in three land modes with different observation strategies, strip widths, and spatial resolutions: IW mode (width 250 km, resolution 5 m × 20 m), wave mode (WM) (width 20 km × 20 km, resolution 5 m × 5 m), and strip mode (SM) (width 80 km, resolution 5 m × 5 m) [59].

For this study, a total of 42 images of Sentinel-1 interference wide (IW) mode ground-range detected data (GRD) (29 scans of the WeiFang site and 13 scans of the Ji'An site) were downloaded from the Alaska Satellite Facility (ASF) website. In addition, Sentinel-2 data in the same period were collected for visual comparison.

2.2.2. Landsat Dataset on GEE

Landsat, a joint program of the USGS and NASA, has been observing the Earth continuously, from 1972 through to the present day [60]. Today, the Landsat satellites image the entire Earth's surface at a 30-m resolution about once every two weeks, including multispectral and thermal data. The Google Earth Engine (GEE) is a cloud computing platform designed by Google Inc., Mountain View, CA, USA [61]. It has been used in global Earth observations and regional-scale surveys, including vegetation mapping and monitoring [56,57,62–64], land-cover mapping [55,65], and agricultural applications [53,66]. Two Landsat collections are available on GEE. Landsat Collection 1 consists of level-1 data products generated from the Landsat 8 operational land imager (OLI)/thermal infrared sensor (TIRS), Landsat 7 enhanced thematic mapper plus (ETM+), Landsat 4–5 thematic mapper (TM), and Landsat 1–5 multispectral scanner (MSS) instruments. Landsat Collection 2 is an improved version made by the USGS. It includes Landsat level-1 data since 1972, as well as level-2 surface reflectance (T1_SR) and surface temperature products from 1982 to the present.

The Landsat Collection 2 data (T1_SR) were used to derive persistent water and non-water distributions over study sites. A total of 1777 scans (965 scans from the WeiFang site and 812 scans from the Ji'An site) were used for calculating historic water probabilities.

2.2.3. GF-3 Data

The GF-3 satellite is the first C-band multi-polarization SAR imaging satellite in China, with a resolution of 1 m and 12 imaging modes [67]. The spatial resolution of GF-3 ranges from 1 to 500 m, and the width ranges from 10 to 650 km, suitable for distinguishing and identifying objects on the ground and at sea.

As an independent test of the model's accuracy, the scene covered by the Gaofen-3 satellite (L2A level, 5 m resolution, HH and HV polarization) in the Ji'An site was selected.

3. Methodology

Our adaptive thresholding method for extracting water coverage (AT-EWC) in flood monitoring was developed, consisting of four steps: the derivation of persistent open-water extent, the pre-processing of SAR data, the extraction of flood coverage, and an accuracy assessment (Figure 2).

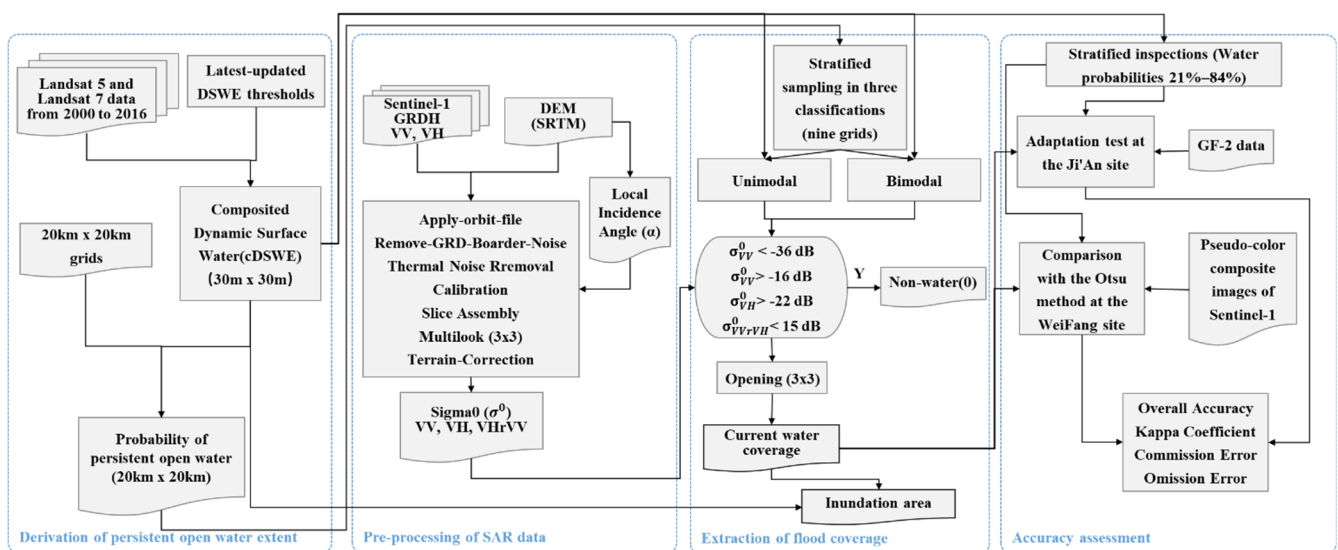


Figure 2. Flowchart showing the processes of our algorithm.

3.1. Derivation of Persistent Open-Water Extent from cDSWE

The DSWE algorithm was used for the derivation of persistent open-water extent. It included five basic decision rules on a series of relatively simple and efficient water detection tests and output the result of each test (one if the condition was satisfied; zero if the condition was not satisfied). The five conditions were combined into a 5-bit output value, ranging from 00000 to 11111, where each number was the result of a specific test (see Appendix A for details). The most recently updated DSWE thresholds were applied [10,25]. In comparative experiments of the two study areas, the updated threshold greatly improved the extraction accuracies of hill shade, land, and urban areas (Figure A1).

In this study, the updated DSWE algorithm was used to calculate Landsat 5 and Landsat 7 data from 2000 to 2016 for both sites to form compositing dynamic surface water extent (cDSWE) products. The class probabilities derived from cDSWE products were used to build prior masks. The data processing was completed using GEE, and data were exported in $1^\circ \times 1^\circ$ tiles for each site. The probability of each class was calculated as:

$$P_{class} = 100 \times N_{occu} / N_{clear-sky} \quad (1)$$

N_{occu} is the number of occurrences of the land, open water, and partial water DSWE classes, and $N_{clear-sky}$ is the number of clear-sky acquisitions from Landsat data.

A link was provided, by which the user can access the GEE script that is used to generate the updated version of the cDSWE dataset (Accessed 1 November 2021) (https://code.earthengine.google.com/5dbba645741ce7d339b978592514d26c?accept_repo=users%2Fbdv%2Fs1flood).

3.2. Pre-Processing of Sentinel-1 SAR Data

The Sentinel-1 ground range-detected (GRD) data acquired in IW modes, with VV and VH backscatter intensity, were divided into $0.5^\circ \times 0.5^\circ$ tiles. This grid system was referenced in the SRTM $1^\circ \times 1^\circ$ data organization system. First, each 1° grid was subdivided into four 0.5° grids to improve the efficiency of pre-processing and post-analysis. Then, on each 0.5° grid, the Sentinel application platform (SNAP) software provided by ESA was used for border noise removal, thermal noise removal, and radiometric calibration. Then, the image pixels were multi-looked to 30 m square and resampled with a bilinear approach to match the Landsat Universal Transverse Mercator (UTM) coordinate system. The recently released STRM 1 arc-second (~ 30 m) digital elevation model (DEM) for terrain correction was used. The step of “terrain flattening” was omitted because the study area

was in a plains area and the terrain was flat; therefore, it did not affect the results of water extraction. On the other hand, adding this step would slow down the overall preprocessing process. This was in contradiction to the efficiency that we sought for the proposed method. The pre-processed images are shown in Figure 3.

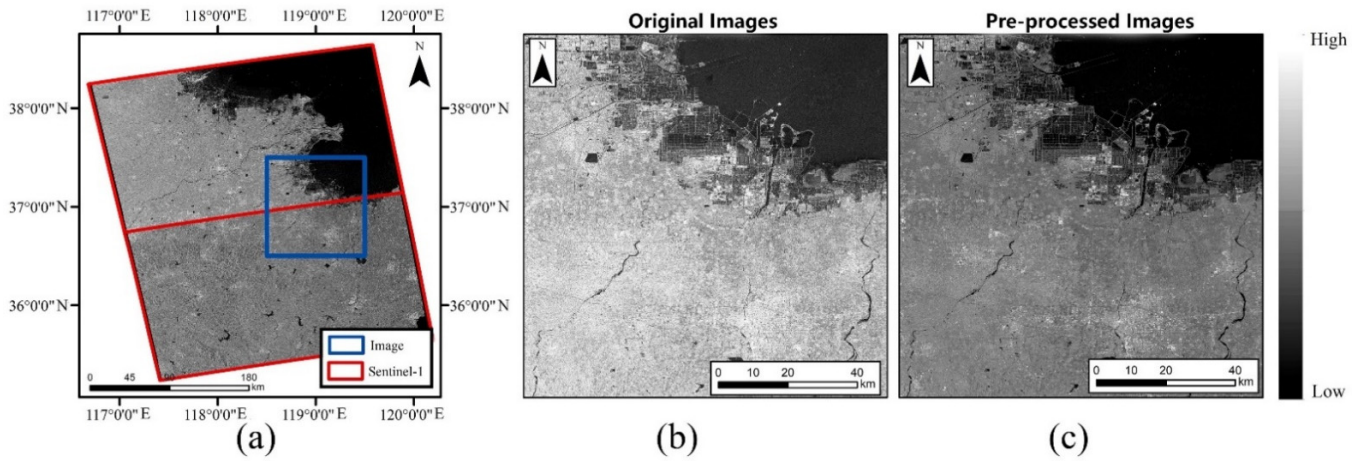


Figure 3. The pre-processing process for Sentinel-1 data. (a) Location of the study area, (b) original image, (c) pre-processed images.

3.3. Extraction of Flood Coverage

After the pre-processing was completed, water was extracted using our proposed automatic thresholding method. It consists of the following four main steps. First, the 30 m cDSWE was aggregated to 20 km grids. Particularly, the proportion of water area within each 20 km grid was calculated using the cDSWE with 30 m-resolution. Then, stratified sampling was used to randomly select three grids in three classifications (high > 66%; medium, 33–66%; low, 0–33%, respectively). A total of nine grids for the three classes were chosen for calculating the thresholds (Figure A2).

Second, the cDSWE was used to determine the histogram type and the threshold value. According to the probability of water area calculated by cDSWE, water was classified into three classes—persistent water, persistent land, and partial (water: 45–100%; land: 1–20%; partial: 21–44%)—and the percentage of each class (N_W , N_L , N_P) was calculated at the same time. In an image with some small water bodies (inland watersheds with few lakes) or little land coverage, the histogram showed unimodally ($N_P \leq \alpha N_W + \beta N_L$); when the proportion of land to water was close, the histogram showed bimodally ($N_P > \alpha N_W + \beta N_L$) (Figure 4). The relationship between the water body probability and the histogram type was obtained by determining the value of α , β . The histogram was unimodal because of the large difference between the area of the water body and the land in the image, so we further classified the unimodal histogram into two situations ($N_W > N_L$ and $N_W < N_L$). Thus, the threshold value was automatically calculated; the specific formula of the threshold for each 20 km grid (T) was as follows:

$$T = \begin{cases} H_{valley}, N_P > \alpha N_W + \beta N_L \\ \mu + 3\sigma, N_P \leq \alpha N_W + \beta N_L, N_W > N_L \\ \mu - 3\sigma, N_P \leq \alpha N_W + \beta N_L, N_W < N_L \end{cases} \quad (2)$$

N_W , N_L , N_P are the proportion of water, land, and partial, respectively; H_{valley} is the valley of the histogram; α , β are adjustable factors; and μ , σ are the mean and variance, respectively.

Next, the thresholds in three bands (T_{VV} , T_{VH} , T_{VVrVH}) were determined using the threshold calculated with Formula (2) using each selected grid (T_{VVi} , T_{VHi} , T_{VVrVHi}), with the following equation:

$$\begin{cases} T_{VV} > \text{mean}(T_{VV_i}) \\ T_{VH} > \text{mean}(T_{VH_i}) \\ T_{VVrVH} > \max(T_{VVrVH_i}) \end{cases} \quad (3)$$

T_{VV} , T_{VH} , T_{VVrVH} denote the threshold values of the VV, VH, and VVrVH bands, respectively, while T_{VV_i} , T_{VH_i} , T_{VVrVH_i} are the thresholds of the selected nine grids.

The morphological opening using a 3×3 square structuring element was used to eliminate noise and fragmented water, and then spliced into $1^\circ \times 1^\circ$ tiles according to the selected date. The output product was in the form of a GeoTIFF without geographic projection, and the resolution was approximately 25 m in the mid-latitude area.

Finally, the persistent open-water extent obtained in Section 3.1, and the results obtained in the above steps, were superimposed to calculate the inundation area:

$$R_I = R_W - R_P \quad (4)$$

R_W is the water extracted from images and R_P is the range of the persistent open-water extent.

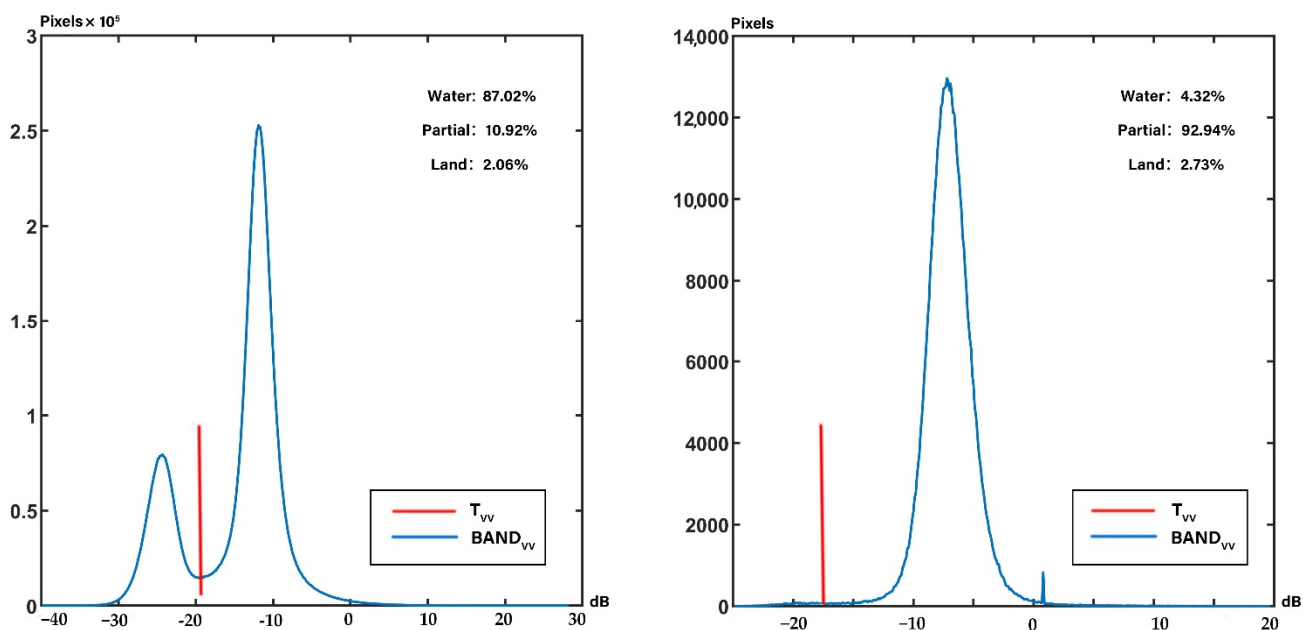


Figure 4. Two types of histograms for images (Band VV). The red line is the determined threshold of the VV band and the blue line is the grayscale curve of that threshold.

3.4. Accuracy Assessment

Based on the available validation dataset at the sites, the accuracy of the results was evaluated. For a quantitative evaluation, four indicators were selected: overall accuracy, kappa coefficient, and the commission and omission of errors.

For the Ji'An site, a stratified inspection was more appropriate but it did not meet the requirements because of the small range of 21–84% probability, so it was not suitable for the stratified sampling test. In addition, it was established that there is a GF-3 image in the Ji'An site from nearly the time of the flood occurrences (access date 10 June 2019, three days apart from the Sentinel-1 data). Thus, 200 points (24 points of water and 176 points of land) in the common area of the two images for the test were randomly selected (Figure 5a). GF-3 images were also used for visual inspection.

For the WeiFang site, 200 points were randomly selected for evaluation, enabling stratified inspections in areas from Landsat-derived cDSWE class probabilities (21–84%). Unlike the Ji'An site, there were no eligible high-resolution images. Thus, a visual inspection of the pseudo-color composite image of Sentinel-1 was performed (Figure 5b).

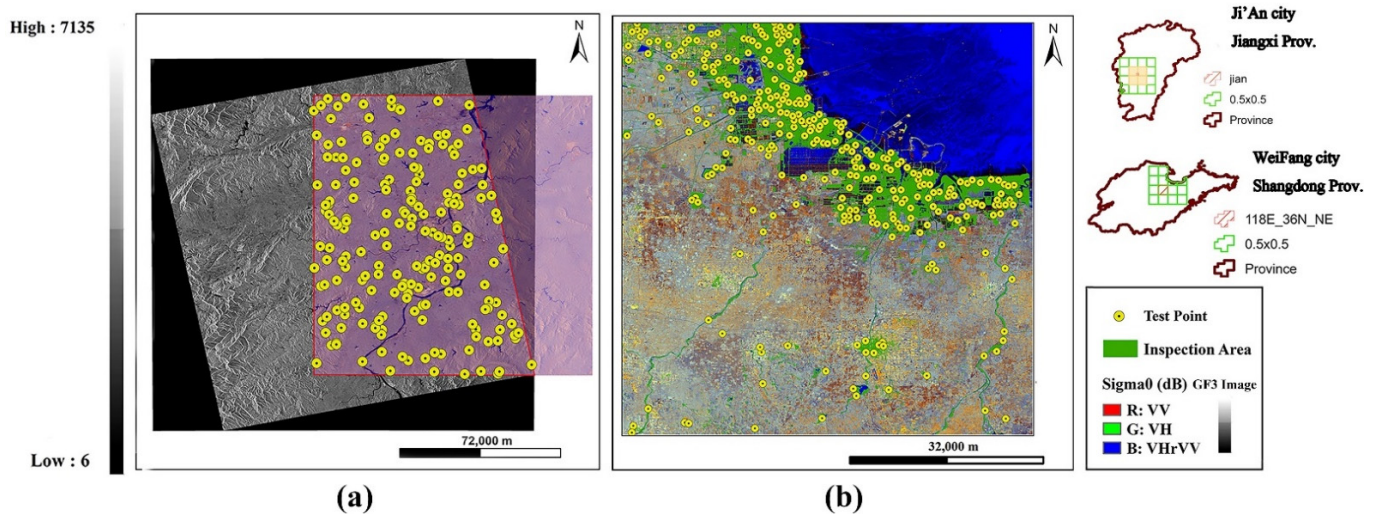


Figure 5. Locations of 200 random points sampled at each of the two sites for visual inspection of the extraction results of the AT-EWC method (Ji'An (a) and WeiFang (b)).

4. Results

4.1. Time-Series Classification of Water and Non-Water

To determine a universal adaptability threshold, nine grids for the three classifications (high > 66%, medium 33–66%, low 0–33%) of the WeiFang site (15 June 2018) were used to calculate thresholds, using the method explained in Section 3.3. They were calculated according to Formulae (2) and (3). In this experiment, the 20 km grids of the WeiFang site were analyzed. This shows that the type of the histogram can be accurately judged when the value of coefficients α , β are set to 3. Finally, the three thresholds were determined as follows:

- First, if $\sigma_{VV}^0 > -16$ dB, mark as water.
- Second, if $\sigma_{VH}^0 > -22$ dB, mark as water.
- Third, if $\sigma_{VVrVH}^0 < 15$ dB, mark as water.

To validate the universality of the threshold, water areas were extracted during the flood period at two sites. The overall results are shown in Figure 6. The detailed results during the flood at both sites were assessed via a time-series analysis. To simulate the water level changes at the WeiFang site, the six images during the flood events of the Fushan Reservoir were separately analyzed (21 July–1 September 2018) (Figure 7a). According to relevant reports, the Fushan Reservoir did not discharge floodwaters downstream during this period, and its area was significantly changed after the flood. At the Ji'An site, three images from 1 June 2019 were analyzed (Figure 7b). The image that was taken on 13 June 2019 revealed a widened river surface with some submerged areas. The three sub-panels reflected the situation before, during, and after the flood, respectively. Comparing the images of the two sites, the flooding lasted longer at the WeiFang site than at the Ji'An site, and the data downloaded from the former failed to monitor its recovery. At the Ji'An site, the incident was monitored from onset to recovery.

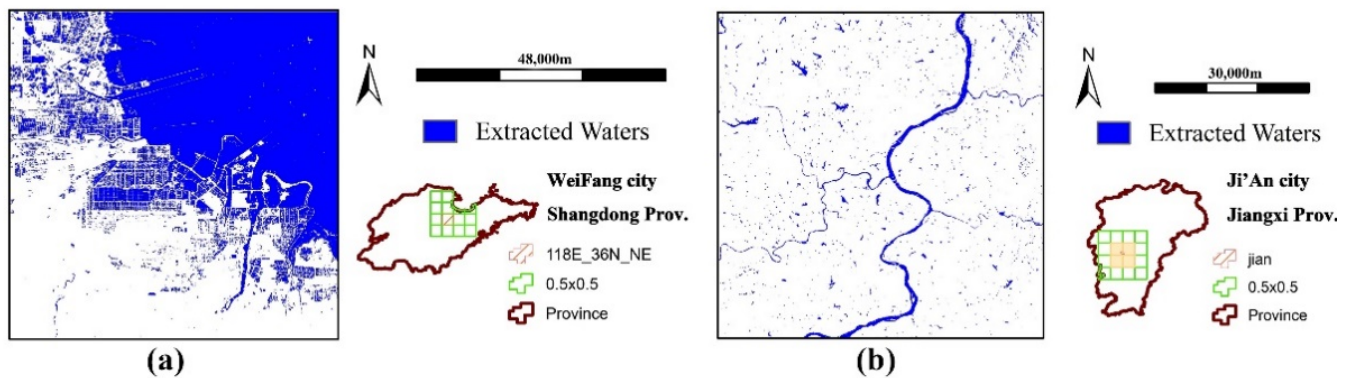


Figure 6. Water extraction results at the WeiFang site on 26 August 2018 (a) and Ji'An site on 25 June 2019 (b).

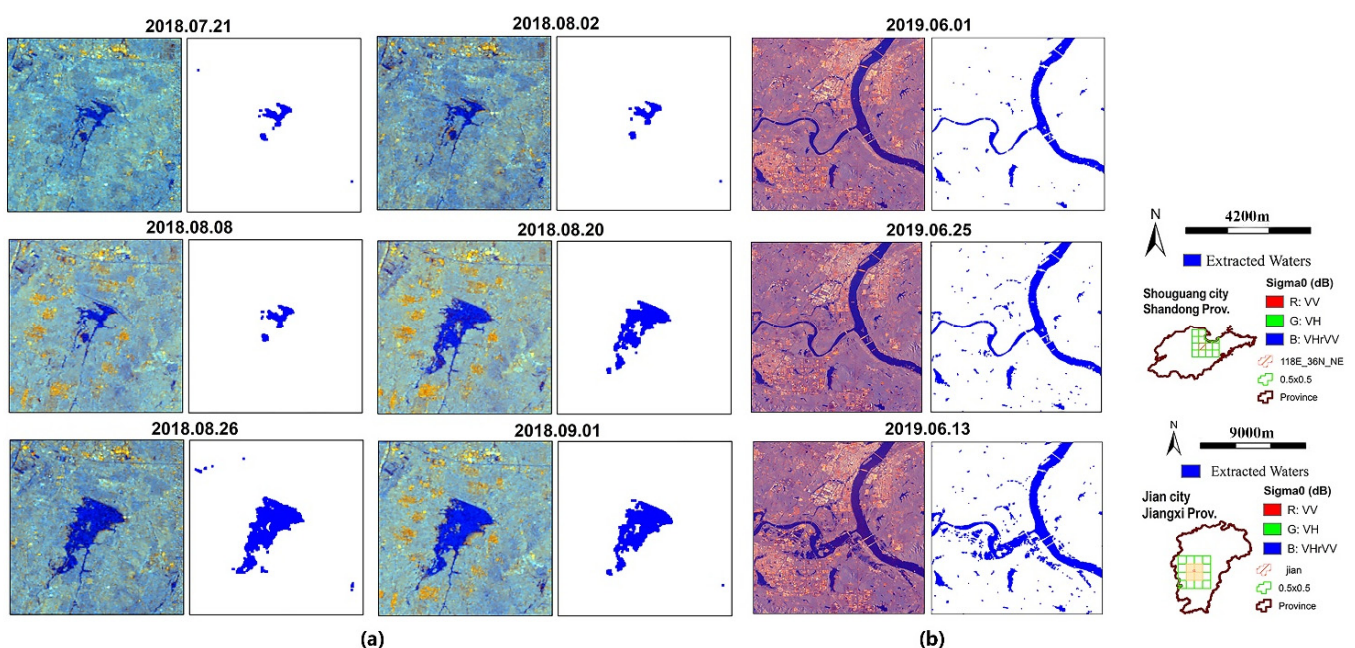


Figure 7. Water level changes in the Fushan Reservoir during the flood event at the WeiFang site (a), and changes in the river during the entire flood event at the Ji'An site (b). At each date, the left image is the false-color composite image from Sentinel-1 data, and the right image shows the extracted water bodies.

4.2. Inundation Range over Flood Event

To assess the impact of a flood event, the inundation range with time-series imagery during the flood event was calculated. Based on the three water body classifications proposed in Section 3.3 (water: 45–100%, land: 1–20%, partial: 21–44%), water bodies with grayscale codes above 45% were selected as the persistent waters. The result was superimposed with the water surface during the flood period assessed in Section 4.1 and the disaster range of the flood event was then estimated (Figure 8). To simulate the inundation range at the WeiFang site, the six images taken during the flood events of the BaiLangHei Reservoirs were separately analyzed (21 July–1 September 2018). Figure 8 shows that the flooding started on 2 August and then gradually expanded until it reached its peak on 20 August. In the two subsequent monitoring images, the inundation extent of the flood decreased. By 1 September, the cessation of flooding could not be detected, which may have been caused by the breach of the more severely affected reservoir. This could simulate the damage to a certain extent.

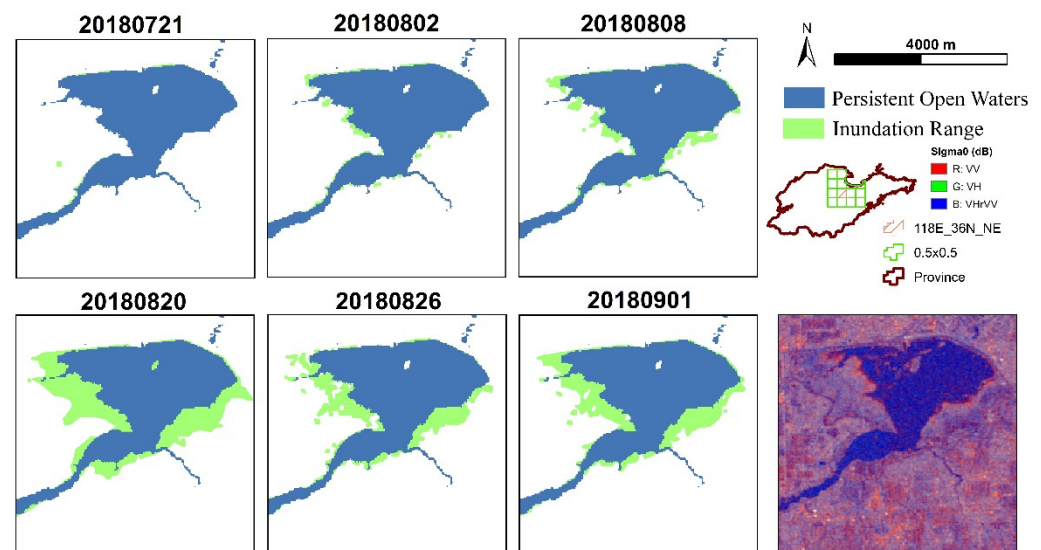


Figure 8. Inundation range at the WeiFang site during the flood period. The blue portion represents the persistent open water. The green portion indicates the inundation range. The image on the right is a Sentinel-1 image from 21 July 2018.

4.3. Accuracy Assessment at Two Sites

4.3.1. Adaptation of the Proposed Thresholds at the Ji'An Site

To quantitatively measure the suitability of the proposed template at the Ji'An site, a visual inspection was conducted at the site using the GF-3 images from June 10. The results show that the metrics obtained using our proposed thresholds for the Ji'An site also perform well (Table 2). The overall accuracies of our algorithm (94.5–96%) were similar in the three periods. The kappa coefficient ranged from 0.74 to 0.81, and the commission and omission errors of the water ranged from 16% to 26%, while those of the land ranged from 1% to 3%. Moreover, the six indicators for 13 June are better than for the other two dates. This may be due to our selection of high-resolution images closest to that date.

Therefore, pseudo-color composite images of Sentinel-1 were used (Table 2). The overall accuracies were above 95.0%. The kappa coefficient ranged from 0.77 to 0.84; the commission and omission errors of the water ranged from 12% to 19%, while those of the land ranged from 1% to 2%. This indicates that our classification accuracy for land is higher than that for water bodies. The data for 13 June continues to yield the best results.

Table 2. Accuracy estimate of the Ji'An site using GF-3.

Data	Overall Accuracy	Kappa Coefficient	Commission Error		Omission Error	
			Land	Water	Land	Water
1 June 2019	95.00%	0.7715	3.41%	16.67%	2.30%	23.08%
13 June 2019	96.00%	0.8172	2.84%	12.50%	1.72%	19.23%
25 June 2019	94.50%	0.7443	3.95%	17.39%	2.30%	26.92%

4.3.2. Comparison with the Otsu Method at the WeiFang Site

To further test our proposed threshold, the results of images from the WeiFang site on 26 August 2018 were compared using the Otsu method. Table 3 showed that the difference between our proposed method regarding the global image and the high group in terms of overall accuracy was 0.01. The differences in the other three evaluation metrics were also small and were controlled within 0.05. However, in the low group and medium group images of a 20 km × 20 km block, the classification results of our method were significantly better than those using the Otsu method, especially in the two sets of comparison results for medium and low groups. In the experiments of the medium group, the overall accuracies

were 96% and 84%, respectively, with a difference of 0.12, and the kappa coefficients were about 0.2. However, it was found that the land commission error and water omission error of the two methods were similar, except that the land commission error and water omission error differed significantly, with the difference of -0.29 (9.63% vs. 38.16%) and -0.16 (3.33% vs. 19.33%), respectively. In the low group, the difference between the two methods was more obvious. The difference in overall accuracy was 0.17. The other five metrics also showed the same pattern as the medium group. This indicated that our method had better accuracy on small blocks. Moreover, the values of the four experimental groups were increasing as the area of water decreased, which indicated that the smaller the area of water in the image to be classified, the more obvious the something of our proposed method. It further illustrated the superiority of our method in areas with smaller bodies of water. Specifically, the two methods had a similar classification accuracy for water bodies, but the Otsu method for land showed less sensitivity.

Table 3. Accuracy estimate of Ji'An site using Sentinel-1.

Data	Overall Accuracy	Kappa Coefficient	Commission Error		Omission Error	
			Land	Water	Land	Water
1 June 2019	95.00%	0.7790	2.87%	19.23%	2.87%	19.23%
13 June 2019	96.50%	0.8427	2.29%	12.00%	1.72%	15.38%
25 June 2019	95.50%	0.7978	2.86%	16.00%	2.30%	19.23%

Figure 9 showed the classification images of the two methods. In addition, in terms of efficiency, the computation time of both methods showed that the proposed method was more efficient (Table 4). The average computation time of our method was 0.1 s, while the comparison of the Otsu method was 0.25 s (Table 5). In all nine sets of test experiments, the AT-EWC method outperformed the Otsu method in terms of speed.

Table 4. Comparison with Otsu method for the WeiFang site.

Type	Threshold	Overall Accuracy	Kappa Coefficient	Commission Error		Omission Error	
				Land	Water	Land	Water
Image	AT-EWC	95.50%	0.9080	3.57%	2.65%	3.57%	2.65%
	Otsu	94.50%	0.8876	4.39%	6.98%	5.22%	5.88%
	(-)	(0.01)	(0.02)	(-0.01)	(-0.04)	(-0.02)	(-0.03)
20 km × 20 km Block (High)	AT-EWC	96.00%	0.9199	2.91%	5.15%	4.76%	3.16%
	Otsu	95.00%	0.8997	4.76%	5.26%	4.76%	5.26%
	(-)	(0.01)	(0.02)	(-0.02)	(0.00)	(0.00)	(-0.02)
20 km × 20 km Block (Middle)	AT-EWC	96.00%	0.8947	2.03%	9.62%	3.33%	6.00%
	Otsu	84.00%	0.6364	2.42%	38.16%	19.33%	6.00%
	(-)	(0.12)	(0.26)	(0.00)	(-0.29)	(-0.16)	(0.00)
20 km × 20 km Block (Low)	AT-EWC	97.50%	0.8697	1.12%	13.64%	1.68%	9.52%
	Otsu	81.00%	0.4136	0.69%	66.07%	20.56%	5.00%
	(-)	(0.17)	(0.46)	(0.00)	(-0.52)	(-0.19)	(0.05)

Table 5. Validation of efficiency between AT-EWC and Otsu.

Time(s)	#1 *	#2	#3	#4	#5	#6	#7	#8	#9	Average
AT-EWC	0.09	0.09	0.11	0.09	0.09	0.09	0.09	0.09	0.19	0.10
Otsu	0.29	0.26	0.24	0.23	0.23	0.23	0.25	0.29	0.24	0.25

* all sub-image tiles have the same size—4000 by 4000 pixels.

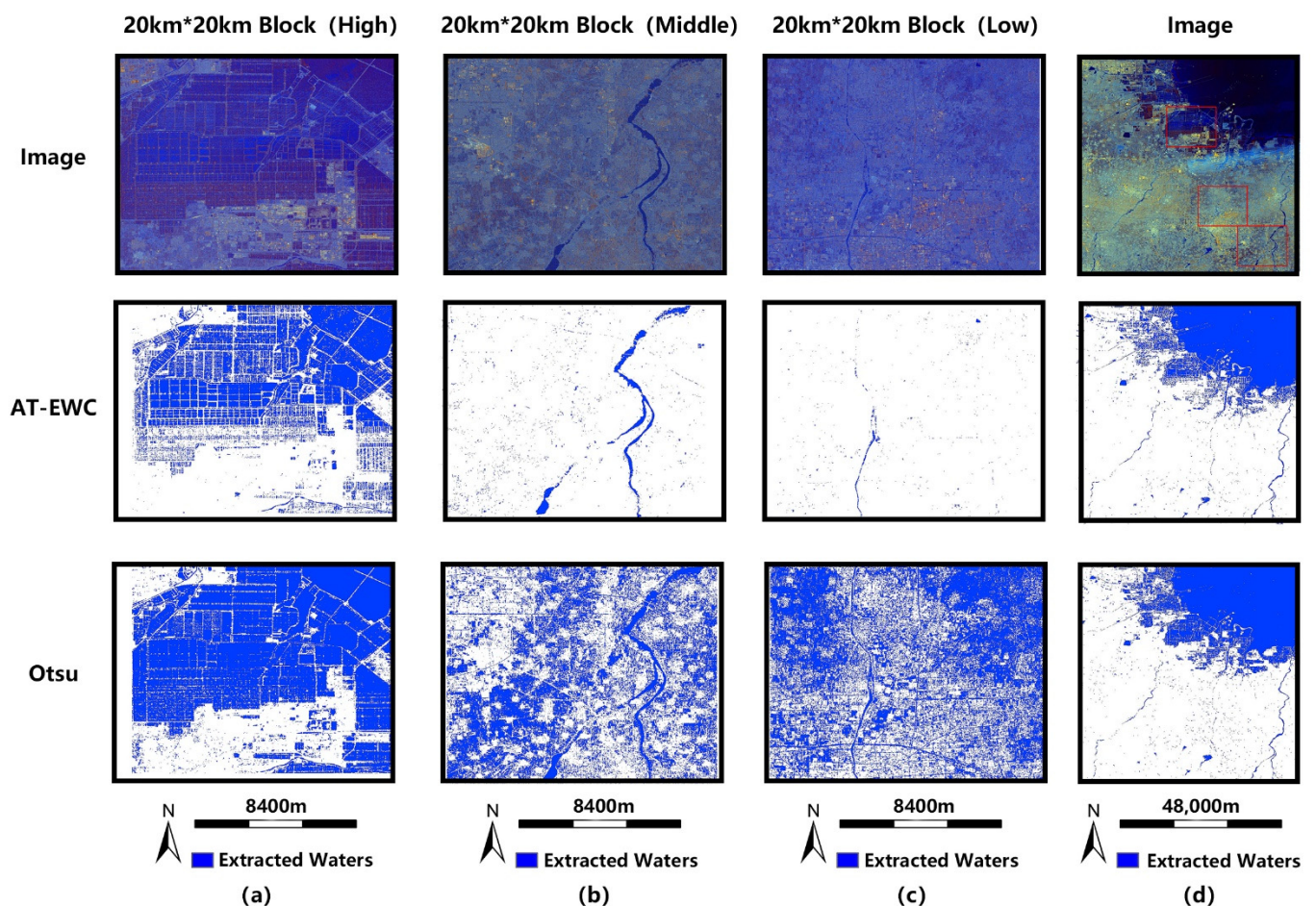


Figure 9. Comparison with Otsu method at the WeiFang site. (a) 20 km × 20 km block (high) (b) 20 km × 20 km block (medium) (c) 20 km × 20 km block (low) (d) 4000 by 4000 pixels image.

5. Discussion

5.1. Significance of This Study

An adaptive thresholding method was proposed for extracting water coverage (AT-EWC) for flood monitoring with the assistance of cDSWE. The probability of persistent water and non-water were first aggregated from cDSWE at a 30-m resolution to a 20 km × 20 km grid system for stratified sampling. Then, cDSWE was further used to assist in determining the shape of the image histogram and generating flood products. Our method responded well to the change of water surface before and after the flood. Specifically, there are three significant outcomes.

First, a fully-automated thresholding method was developed for extracting flood ranges with higher temporal resolution. Because Sentinel-1 data has been provided since 2014, few studies have explored large-scale and multi-temporal water monitoring through optical remote sensing products (e.g., Landsat). Moreover, most of the existing water monitoring products comprise annual composite data. The inundation area during the flood time can be established by our method, which makes up for the low temporal resolution achieved by optical products. Moreover, our method is completely automated, and there is no human influence on the process.

Second, good adaptability has been shown on two different types of sites. Our proposed thresholds that were calculated at the WeiFang site were used at the Ji'An site, where they also demonstrated good adaptability. From our experimental results in Tables 1 and 2, the overall accuracy of the results reached 96.5% and the kappa coefficient remained at around 0.8. This indicated that our proposed thresholds can be applied to other regions. From the comparison results of the three sets of experiments, the accuracy of 1 June and 25

June was relatively lower compared to June 3. This indicates that our proposed thresholds are not only adaptable to all regions but also have better extraction accuracy during floods.

Third, in terms of accuracy and efficiency, our proposed method demonstrated excellent performance. In the block with the low and medium probability of water, the Otsu method showed obvious shortcomings, and the overall accuracy was around 80%, which is much lower than its classification accuracy on the image. In contrast, our method performed well in the classification results in the above four types. The Otsu method used the image histogram for the calculation of maximum interclass variances. This worked well in the case of bimodal image histograms. However, in the unimodal case, the Otsu method showed poor performance where there were inland watersheds with few lakes. Thus, Otsu's shortcomings in small water bodies were improved by the AT-EWC method. Table 4 showed that our algorithm outperforms the Otsu method in terms of computation time. This indicates that our method is more efficient and meets the time-sensitive needs of flood monitoring well.

5.2. Limitations and Potential Improvements

The proposed method can automatically extract the extent of water and meet the accuracy requirements for water extraction. It also gives an excellent performance in small water bodies. Radar signals over still water are close to zero due to specular reflection. While the VV backscatter intensities appear corrugated over the windy surface, since the Ji'An site is an inland basin, there is no ripple on the SAR images. There are also no obvious waves on the image of the WeiFang site. Therefore, we do not discuss the influence of windy surfaces in terms of our method, which might prove an issue elsewhere. There are also improvements in using historical water-body data to determine the type of histogram. Specifically, the determination of parameters α and β was obtained from our calculations for the WeiFeng site. Although the adaptation of the proposed thresholds at the Ji'An site was demonstrated, we have not tested it in other, larger areas. On the other hand, the cDSWE product itself also shows improvements in accuracy.

In future experiments, we will continue to investigate the relationship between historical water and image histograms. Specifically, the value of the parameters α and β needs to be determined by more experiments. Other datasets, such as GSW and G3WBM, will be analyzed and compared to address the shortcomings of thresholds judged using a single dataset. Experiments will be conducted from the following three aspects.

First, a longer period of Landsat data will be used to calculate persistent open-water extent. A total of 16 years of Landsat data were used for the composite cDSWE products to calculate the area of persistent open-water extent. In the future, we will try to use longer-term data for experiments to improve the accuracy of our method. Longer-term data may lead to more suitable coefficients, thus improving the accuracy of the method.

Second, other datasets, such as GSW and G3WBM, will be tested, and it will be considered whether these datasets can be combined to improve accuracy. Only cDSWE products were used to calculate the probability of water bodies in our method. However, a variety of global water datasets are provided to scholars for research. It is possible that multiple water datasets, when combined, could improve the coefficients and algorithm.

Third, the proposed method (AT-EWC) will be applied to a larger area. In this paper, the determination of parameters α and β was obtained from our calculations for the WeiFeng site. Although the adaptation of the proposed thresholds at the Ji'An site was demonstrated, whether our method still performs well for a larger area needs to be verified. We will also conduct algorithm tests in other research areas in the future.

6. Conclusions

In this study, an adaptive thresholding method for extracting water coverage (AT-EWC) in response to rapid flooding was proposed that automatically and quickly derives a classification map of the water and non-water areas. In addition, the inundation area was calculated with the assistance of persistent water extent information from cDSWE.

Particularly, the shapes of the gray histogram were classified using prior water distribution information from long-term Landsat data. The algorithm implemented a fully automated process, from water extraction and determination to the output of the results. Moreover, most of the existing water products use annual composite data. Our method makes up for the low temporal resolution of optical products. In terms of accuracy and efficiency, the proposed method achieved better results in some small water bodies (inland watersheds with few lakes) than the Otsu [6] algorithm. It ameliorated the problem that the Otsu algorithm does not have high classification accuracy in small areas. Moreover, because the proposed method improved the threshold determination, it completed calculations faster than the existing methods and satisfies the needs of rapid flood disaster monitoring.

In future experiments, we will continue to investigate the relationship between historical water data and image histogram types to improve the AT-EWC method for assessing rapid flood inundation. We will study possible improvements, from the time period of the water dataset to the diversity of the dataset, and the area to which the AT-EWC method is applied.

Author Contributions: W.H. designed the experiments. S.C. processed the data and wrote the manuscript. M.F. prepared the Landsat data and assisted in algorithm development. W.H. and Y.C. reviewed and edited the first draft of the manuscript. All authors assisted in revising the manuscript. All authors have read and agreed to the published version of the manuscript.

Funding: This work is supported by the National R&D Program of China under Grant 2018YFB2100504, the Open Fund of Key Laboratory of Urban Land Resources Monitoring and Simulation, Ministry of Natural Resources under Grant number KF-2020-05-0076, and the Starter Talent Research Program of Wuhan University (413000067, 413000085).

Data Availability Statement: Not applicable.

Acknowledgments: We would like to thank ESA's Sentinels Scientific Data Hub, through the Copernicus mission, that provided the Sentinel-1 SAR data. We give special thanks to Google's Earth Engine which provided the archived Landsat data, as well as computation capabilities. We thank two anonymous reviewers whose constructive comments led to an improved description of our introduction and methodology.

Conflicts of Interest: The authors declare no conflict of interest. The funders had no role in the design of the study; in the collection, analyses, or interpretation of data; in the writing of the manuscript, or in the decision to publish the results.

Appendix A

The DSWE algorithm was implemented by the following steps:

- First, determine the latitude and longitude of the study area and the time of using the data; import the used data; set the name of the save folder.
- Second, write a function that calculates the water body index (MNDWI, NDVI, MBSR, AWESH). The arguments of this function are calculated as follows:
 - (a) Modified Normalized Difference Wetness Index (MNDWI) = $(\text{green} - \text{SWIR1}) / (\text{green} + \text{SWIR1})$
 - (b) Multi-band Spectral Relationship Visible (MBSRV) = $\text{green} + \text{red}$
 - (c) Multi-band Spectral Relationship Near-Infrared (MBSRN) = $\text{NIR} + \text{SWIR1}$
 - (d) Automated Water Extent Shadow (AWESH) = $\text{blue} + (2.5 \times \text{green}) - (1.5 \times \text{MBSRN}) - (0.25 \times \text{SWIR2})$
 - (e) Normalized Difference Vegetation Index (NDVI) = $(\text{NIR} - \text{red}) / (\text{NIR} + \text{red})$
- Third, encode the five basic experimental functions of the DSWE algorithm.
- Forth, in the code, write three classification functions corresponding to Water (Pixel Value = 1 and 2), Land (Pixel Value = 0) and Potential (Pixel Value = 3).
- Fifth, output the final classification result to Google Drive.

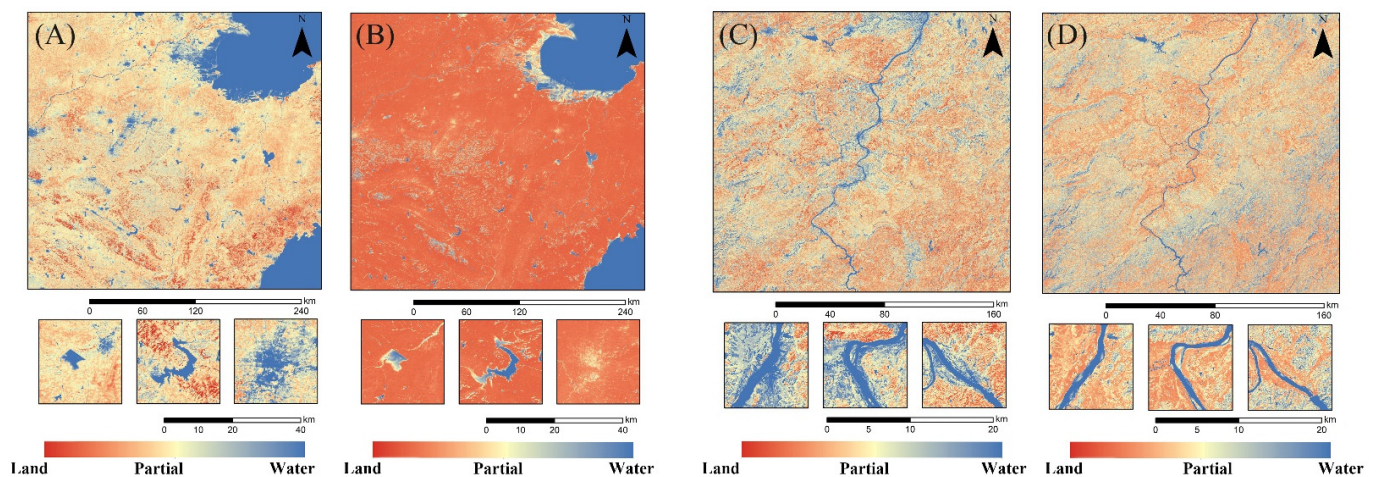


Figure A1. Comparison of the old and new versions of cDSWE (v1 (A,B) and v3 (C,D)).

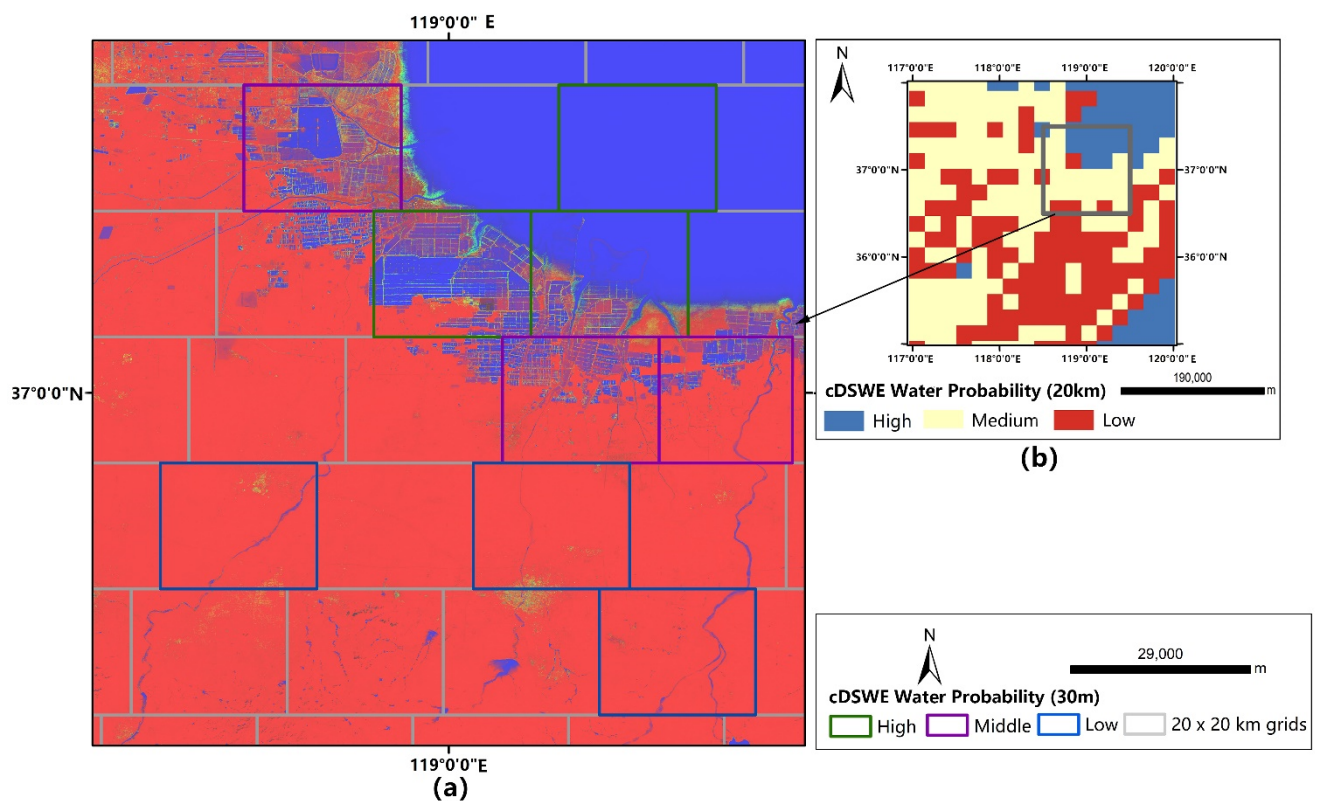


Figure A2. The location of the selected nine grids. (a) Location of sample block; (b) the WeiFang study site.

References

- Goldberg, M. The Transition from Current Atmospheric Measurements to the NPOESS Era. In *AGU Fall Meeting Abstracts*; 2005. Available online: https://www.researchgate.net/publication/241370237_The_Transition_from_Current_Atmospheric_Measurements_to_the_NPOESS_Era (accessed on 25 October 2021).
- Voigt, S.; Giulio-Tonolo, F.; Lyons, J.; Kučera, J.; Jones, B.; Schneiderhan, T.; Platzeck, G.; Kaku, K.; Hazarika, M.K.; Czarán, L.; et al. Global trends in satellite-based emergency mapping. *Science* **2016**, *353*, 247–252. [[CrossRef](#)]
- Ritchie, J.C.; Schiebe, F.R.; Mchenry, J.R. Remote Sensing of Suspended Sediments in Surface Water. *Photogramm. Eng. Remote Sens.* **1976**, *42*, 1539–1545.
- Du, J.; Kimball, J.S.; Galantowicz, J.; Kim, S.B.; Chan, S.K.; Reichle, R.; Jones, L.A.; Watts, J.D. Assessing global surface water inundation dynamics using combined satellite information from SMAP, AMSR2 and Landsat. *Remote Sens. Environ.* **2018**, *213*, 1–17. [[CrossRef](#)]
- Wulder, M.A.; Masek, J.G.; Cohen, W.B.; Loveland, T.R.; Woodcock, C.E. Opening the archive: How free data has enabled the science and monitoring promise of Landsat. *Remote Sens. Environ.* **2012**, *122*, 2–10. [[CrossRef](#)]

6. Otsu, N. A threshold selection method from gray-level histograms. *IEEE Trans. Syst. Man Cybern.* **1979**, *9*, 62–66. [[CrossRef](#)]
7. Wu, H.; Liu, C.; Zhang, Y.; Sun, W. Water feature extraction from aerial-image fused with airborne LIDAR data. In Proceedings of the 2009 Joint Urban Remote Sensing Event, Shanghai, China, 20–22 May 2009.
8. Feng, M.; Sexton, J.O.; Channan, S.; Townshend, J.R. A global, high-resolution (30-m) inland water body dataset for 2000: First results of a topographic–spectral classification algorithm. *Int. J. Digit. Earth* **2016**, *9*, 113–133. [[CrossRef](#)]
9. Pickens, A.H.; Hansen, M.C.; Hancher, M.; Stehman, S.V.; Tyukavina, A.; Potapov, P.; Marroquin, B.; Sherani, Z. Mapping and sampling to characterize global inland water dynamics from 1999 to 2018 with full Landsat time-series. *Remote Sens. Environ.* **2020**, *243*, 111792. [[CrossRef](#)]
10. Jones, J.W. Improved Automated Detection of Subpixel-Scale Inundation—Revised Dynamic Surface Water Extent (DSWE) Partial Surface Water Tests. *Remote Sens.* **2019**, *11*, 374. [[CrossRef](#)]
11. Pekel, J.-F.; Cottam, A.; Gorelick, N.; Belward, A.S. High-resolution mapping of global surface water and its long-term changes. *Nature* **2016**, *540*, 418–422. [[CrossRef](#)]
12. Yamazaki, D.; Trigg, M.A.; Ikeshima, D. Development of a global ~90m water body map using multi-temporal Landsat images. *Remote Sens. Environ.* **2015**, *171*, 337–351. [[CrossRef](#)]
13. Tholey, N.; Clandillon, S.; Fraipont, P.D. The contribution of spaceborne SAR and optical data in monitoring flood events: Examples in northern and southern France. *Hydrol. Process.* **1997**, *11*, 1409–1413. [[CrossRef](#)]
14. Solbo, S.; Pettinato, S.; Paloscia, S.; Santi, E.; Brusotti, P.; Solheim, I. Mapping of flooding in the Alessandria area with ERS. In Proceedings of the IGARSS 2004. 2004 IEEE International Geoscience and Remote Sensing Symposium, Anchorage, AK, USA, 20–24 September 2004.
15. Bartsch, A.; Wagner, W.; Scipal, K.; Pathe, C.; Sabel, D.; Wolski, P. Global monitoring of wetlands—The value of ENVISAT ASAR Global mode. *J. Environ. Manag.* **2009**, *90*, 2226–2233. [[CrossRef](#)]
16. Hess, L.; Melack, J.; Filoso, S.; Wang, Y. Delineation of inundated area and vegetation along the Amazon floodplain with the SIR-C synthetic aperture radar. *IEEE Trans. Geosci. Remote Sens.* **1995**, *33*, 896–904. [[CrossRef](#)]
17. Henry, J.B.; Chastanet, P.; Fellah, K.; Desnos, Y.L. Envisat multi-polarized ASAR data for flood mapping. *Int. J. Remote Sens.* **2006**, *27*, 1921–1929. [[CrossRef](#)]
18. Martinis, S.; Kersten, J.; Twele, A. A fully automated TerraSAR-X based flood service. *ISPRS J. Photogramm. Remote Sens.* **2015**, *104*, 203–212.
19. Mason, D.C.; Speck, R.; Devereux, B.; Schumann, J.P.; Neal, J.C.; Bates, P.D. Flood Detection in Urban Areas Using TerraSAR-X. *IEEE Trans. Geosci. Remote Sens.* **2010**, *48*, 882–894. [[CrossRef](#)]
20. Mason, D.C.; Davenport, I.J.; Neal, J.C.; Schumann, J.P.; Bates, P.D. Near Real-Time Flood Detection in Urban and Rural Areas Using High-Resolution Synthetic Aperture Radar Images. *IEEE Trans. Geosci. Remote Sens.* **2012**, *50*, 3041–3052. [[CrossRef](#)]
21. Tanguy, M.; Chokmani, K.; Bernier, M.; Poulin, J.; Raymond, S. River flood mapping in urban areas combining Radarsat-2 data and flood return period data. *Remote Sens. Environ.* **2017**, *198*, 442–459. [[CrossRef](#)]
22. Pulvirenti, L.; Chini, M.; Pierdicca, N.; Guerriero, L.; Ferrazzoli, P. Flood monitoring using multi-temporal COSMO-SkyMed data: Image segmentation and signature interpretation. *Remote Sens. Environ.* **2011**, *115*, 990–1002. [[CrossRef](#)]
23. Twele, A.; Cao, W.; Plank, S.; Martinis, S. Sentinel-1-based flood mapping: A fully automated processing chain. *Int. J. Remote Sens.* **2016**, *37*, 2990–3004. [[CrossRef](#)]
24. Laurila, P.; Modrzewski, R.; Cheng, T.; Campbell, B.; Yanni, V.G. Validation of ICEYE Small Satellite SAR Design for Ice Detection and Imaging. In Proceedings of the Arctic Technology Conference, St. John’s, NL, Canada, 24–26 October 2016.
25. Huang, W.; DeVries, B.; Huang, C.; Lang, M.W.; Jones, J.W.; Creed, I.F.; Carroll, M.L. Automated Extraction of Surface Water Extent from Sentinel-1 Data. *Remote Sens.* **2018**, *10*, 797. [[CrossRef](#)]
26. Bioresita, F.; Puissant, A.; Stumpf, A.; Malet, J.-P. A Method for Automatic and Rapid Mapping of Water Surfaces from Sentinel-1 Imagery. *Remote Sens.* **2018**, *10*, 217. [[CrossRef](#)]
27. Liu, J.; Li, W.; Tian, Y. Automatic thresholding of gray-level pictures using two-dimension Otsu method. In Proceedings of the International Conference on Circuits and Systems, Shenzhen, China, 16–17 June 1991; Volume 1, pp. 325–327.
28. Stutz, D.; Hermans, A.; Leibe, B. Superpixels: An evaluation of the state-of-the-art. *Comput. Vis. Image Underst.* **2018**, *166*, 1–27. [[CrossRef](#)]
29. Lang, F.; Yang, J.; Yan, S.; Qin, F. Superpixel Segmentation of Polarimetric Synthetic Aperture Radar (SAR) Images Based on Generalized Mean Shift. *Remote Sens.* **2018**, *10*, 1592. [[CrossRef](#)]
30. Ciecholewski, M. River channel segmentation in polarimetric SAR images: Watershed transform combined with average contrast maximisation. *Expert Syst. Appl.* **2017**, *82*, 196–215. [[CrossRef](#)]
31. Cousty, J.; Bertrand, G.; Najman, L.; Couprie, M. Watershed Cuts: Thinnings, Shortest Path Forests, and Topological Watersheds. *IEEE Trans. Pattern Anal. Mach. Intell.* **2010**, *32*, 925–939. [[CrossRef](#)] [[PubMed](#)]
32. Braga, A.M.; Marques, R.C.P.; Rodrigues, F.A.A.; Medeiros, F.N.S. A Median Regularized Level Set for Hierarchical Segmentation of SAR Images. *IEEE Geosci. Remote Sens. Lett.* **2017**, *14*, 1171–1175. [[CrossRef](#)]
33. Jin, R.; Yin, J.; Zhou, W.; Yang, J. Level Set Segmentation Algorithm for High-Resolution Polarimetric SAR Images Based on a Heterogeneous Clutter Model. *IEEE J. Sel. Top. Appl. Earth Obs. Remote Sens.* **2017**, *10*, 4565–4579. [[CrossRef](#)]
34. Kapur, J.N.; Sahoo, P.K.; Wong, A.K.C. A new method for gray-level picture thresholding using the entropy of the histogram. *Comput. Vision, Graph. Image Process.* **1985**, *29*, 273–285. [[CrossRef](#)]

35. Pun, T. A new method for grey-level picture thresholding using the entropy of the histogram. *Signal Process.* **1980**, *2*, 223–237. [[CrossRef](#)]
36. Sahoo, P.K.; Soltani, S.; Wong, A.K.C. A survey of thresholding techniques. *Comput. Vis. Graph. Image Process.* **1988**, *41*, 233–260. [[CrossRef](#)]
37. Sekertekin, A. A Survey on Global Thresholding Methods for Mapping Open Water Body Using Sentinel-2 Satellite Imagery and Normalized Difference Water Index. *Arch. Comput. Methods Eng.* **2021**, *28*, 1335–1347. [[CrossRef](#)]
38. Wang, Z.; Zhang, R.; Zhang, Q.; Zhu, Y.; Huang, B.; Lu, Z. An Automatic Thresholding Method For Water Body Detection From SAR Image. In Proceedings of the 2019 IEEE International Conference on Signal, Information and Data Processing (ICSIDP), Chongqing, China, 11–13 December 2019; pp. 1–4.
39. Liang, J.; Liu, D. A local thresholding approach to flood water delineation using Sentinel-1 SAR imagery. *ISPRS J. Photogramm. Remote Sens.* **2020**, *159*, 53–62. [[CrossRef](#)]
40. Hong, Z.; Fan, J. A Threshold Segmentation Method for Sparse Histogram Image. In Proceedings of the 2009 Sixth International Conference on Fuzzy Systems and Knowledge Discovery, Tianjin, China, 14–16 August 2009; pp. 340–344.
41. Coudray, N.; Buessler, J.L.; Urban, J.P. Robust threshold estimation for images with unimodal histograms. *Pattern Recognit. Lett.* **2010**, *31*, 1010–1019. [[CrossRef](#)]
42. Maniar, H.; Ryali, S.; Kulkarni, M.S.; Abubakar, A. 2018 Machine-learning methods in geoscience. In *SEG Technical Program Expanded Abstracts*; Society of Exploration Geophysicists: Tulsa, OK, USA, 2018; pp. 4638–4642.
43. Shahabi, H.; Shirzadi, A.; Ghaderi, K.; Omidvar, E.; Al-Ansari, N.; Clague, J.J.; Geertsema, M.; Khosravi, K.; Amini, A.; Bahrami, S.; et al. Flood Detection and Susceptibility Mapping Using Sentinel-1 Remote Sensing Data and a Machine Learning Approach: Hybrid Intelligence of Bagging Ensemble Based on K-Nearest Neighbor Classifier. *Remote Sens.* **2020**, *12*, 266. [[CrossRef](#)]
44. Lv, W.; Yu, Q.; Yu, W. Water extraction in SAR images using GLCM and Support Vector Machine. In *IEEE 10th International Conference on Signal Processing Proceedings*; IEEE: Piscataway, NJ, USA, 2010; pp. 740–743.
45. Acharya, T.D.; Subedi, A.; Dong, H.L. Evaluation of Machine Learning Algorithms for Surface Water Extraction in a Landsat 8 Scene of Nepal. *Sensors* **2019**, *19*, 2769. [[CrossRef](#)]
46. Chen, Y.; Fan, R.; Yang, X.; Wang, J.; Latif, A. Extraction of Urban Water Bodies from High-Resolution Remote-Sensing Imagery Using Deep Learning. *Water* **2018**, *10*, 585. [[CrossRef](#)]
47. Tyrallis, H.; Papacharalampous, G.; Langousis, A. A Brief Review of Random Forests for Water Scientists and Practitioners and Their Recent History in Water Resources. *Water* **2019**, *11*, 910. [[CrossRef](#)]
48. An, C.; Niu, Z.; Li, Z.; Chen, Z. Otsu Threshold Comparison and SAR Water Segmentation Result. *J. Electron. Inf. Technol.* **2010**, *32*, 2215–2219. [[CrossRef](#)]
49. Liu, D.; Yu, J. Otsu Method and K-means. In Proceedings of the 2009 Ninth International Conference on Hybrid Intelligent Systems, Shenyang, China, 12–14 August 2009; Volume 1, pp. 344–349.
50. Jia, H.; Sun, K.; Song, W.; Peng, X.; Lang, C.; Li, Y. Multi-Strategy Emperor Penguin Optimizer for RGB Histogram-Based Color Satellite Image Segmentation Using Masi Entropy. *IEEE Access* **2019**, *7*, 134448–134474. [[CrossRef](#)]
51. Nakmuenwai, P.; Yamazaki, F.; Liu, W. Automated Extraction of Inundated Areas from Multi-Temporal Dual-Polarization RADARSAT-2 Images of the 2011 Central Thailand Flood. *Remote Sens.* **2017**, *9*, 78. [[CrossRef](#)]
52. Chini, M.; Hostache, R.; Giustarini, L.; Matgen, P. A Hierarchical Split-Based Approach for Parametric Thresholding of SAR Images: Flood Inundation as a Test Case. *IEEE Trans. Geosci. Remote Sens.* **2017**, *55*, 6975–6988. [[CrossRef](#)]
53. Xiong, J.; Thenkabail, P.S.; Tilton, J.C.; Gumma, M.K.; Teluguntla, P.; Oliphant, A.; Congalton, R.G.; Yadav, K.; Gorelick, N. Nominal 30-m Cropland Extent Map of Continental Africa by Integrating Pixel-Based and Object-Based Algorithms Using Sentinel-2 and Landsat-8 Data on Google Earth Engine. *Remote Sens.* **2017**, *9*, 1065. [[CrossRef](#)]
54. Imandoust, S.B.; Bolandraftar, M. Application of K-nearest neighbor (KNN) approach for predicting economic events theoretical background. *Int. J. Eng. Res. Appl.* **2013**, *3*, 605–610.
55. Mahdianpari, M.; Salehi, B.; Mohammadimanesh, F.; Homayouni, S.; Gill, E. The First Wetland Inventory Map of Newfoundland at a Spatial Resolution of 10 m Using Sentinel-1 and Sentinel-2 Data on the Google Earth Engine Cloud Computing Platform. *Remote Sens.* **2018**, *11*, 43. [[CrossRef](#)]
56. Johansen, K.; Phinn, S.; Taylor, M. Mapping woody vegetation clearing in Queensland, Australia from Landsat imagery using the Google Earth Engine. *Remote Sens. Appl. Soc. Environ.* **2015**, *1*, 36–49. [[CrossRef](#)]
57. Tsai, Y.H.; Stow, D.; Chen, H.L.; Lewison, R.; An, L.; Shi, L. Mapping Vegetation and Land Use Types in Fanjingshan National Nature Reserve Using Google Earth Engine. *Remote Sens.* **2018**, *10*, 927. [[CrossRef](#)]
58. Torres, R.; Snoeij, P.; Geudtner, D.; Bibby, D.; Davidson, M.; Attema, E.; Potin, P.; Rommen, B.; Floury, N.; Brown, M.; et al. GMES Sentinel-1 mission. *Remote Sens. Environ.* **2012**, *120*, 9–24. [[CrossRef](#)]
59. Simmons, A.; Fellous, J.L.; Ramaswamy, V.; Trenberth, K.; Asrar, G.; Balmaseda, M.; Burrows, J.P.; Ciaia, P.; Drinkwater, M.; Friedlingstein, P.; et al. Observation and integrated Earth-system science: A roadmap for 2016–2025. *Adv. Space Res.* **2016**, *57*, 2037–2103. [[CrossRef](#)]
60. Williams, D.L.; Goward, S.; Arvidson, T. Landsat: Yesterday, Today, and Tomorrow. *Photogramm. Eng. Remote Sens.* **2006**, *72*, 1171–1178. [[CrossRef](#)]
61. Gorelick, N.; Hancher, M.; Dixon, M.; Ilyushchenko, S.; Thau, D.; Moore, R. Google Earth Engine: Planetary-scale geospatial analysis for everyone. *Remote Sens. Environ.* **2017**, *202*, 18–27. [[CrossRef](#)]

62. Goldblatt, R.; Rivera Ballesteros, A.; Burney, J. High Spatial Resolution Visual Band Imagery Outperforms Medium Resolution Spectral Imagery for Ecosystem Assessment in the Semi-Arid Brazilian Sertão. *Remote Sens.* **2017**, *9*, 1336. [[CrossRef](#)]
63. Robinson, N.P.; Allred, B.W.; Jones, M.O.; Moreno, A.; Kimball, J.S.; Naugle, D.E.; Erickson, T.A.; Richardson, A.D. A Dynamic Landsat Derived Normalized Difference Vegetation Index (NDVI) Product for the Conterminous United States. *Remote Sens.* **2017**, *9*, 863. [[CrossRef](#)]
64. Hansen, M.C.; Potapov, P.V.; Moore, R.; Hancher, M.; Turubanova, S.A.; Tyukavina, A.; Thau, D.; Stehman, S.V.; Goetz, S.J.; Loveland, T.R.; et al. High-Resolution Global Maps of 21st-Century Forest Cover Change. *Science* **2013**, *342*, 850–853. [[CrossRef](#)] [[PubMed](#)]
65. He, M.; Kimball, J.S.; Maneta, M.P.; Maxwell, B.D.; Moreno, A.; Beguería, S.; Wu, X. Regional Crop Gross Primary Productivity and Yield Estimation Using Fused Landsat-MODIS Data. *Remote Sens.* **2018**, *10*, 372. [[CrossRef](#)]
66. Aguilar, R.; Zurita-Milla, R.; Izquierdo-Verdiguier, E.; De By, R.A. A Cloud-Based Multi-Temporal Ensemble Classifier to Map Smallholder Farming Systems. *Remote Sens.* **2018**, *10*, 729. [[CrossRef](#)]
67. Qiu, X.; Ding, C.; Lei, B.; Han, B.; Li, F. A Novel Proposal of Gaofen-3 Satellite Constellation for Multi-Applications. *ISPRS-Int. Arch. Photogramm. Remote Sens. Spat. Inf. Sci.* **2017**, *XLII-2/W7*, 635–639. [[CrossRef](#)]